J Mater Sci (2006) 41:7862–7871
DOI 10.1007/s10853-006-0605-7

# Superfast densification of nanocrystalline oxide powders by spark plasma sintering

**R. Chaim**

Received: 6 February 2006 / Accepted: 20 June 2006 / Published online: 24 October 2006


**Abstract** Spark plasma sintering (SPS) is a newly discovered old technique which recently has been used for superfast densification of ceramic powders. Simultaneous application of pulsed high dc current densities and load is the necessary condition for rapid and full densification of ceramic powders by SPS. Commercial nanocrystalline magnesium oxide (nc-MgO) and yttrium aluminum garnet (nc-YAG) powders were densified to optical transparency using spark plasma sintering at distinctly different homologous temperatures (0.3 $T_m$ for nc-MgO and 0.7 $T_m$ for nc-YAG). The observed microstructure, density and grain size evolutions versus the SPS temperature were analyzed. The enhanced densification of the nc-MgO powder at the present SPS conditions was related to plastic deformation followed by diffusion processes. Densification of nc-YAG powder was described by the formation of viscous layer at the particle surfaces and corresponding densification by grain rotation and diffusion through the liquid phase. Densification by normal grain growth takes place at higher relative densities, regardless of the material.

## Introduction

Full densification of ceramic powder compacts is an old challenge that has led to the development of new sintering strategies and densification techniques. Spark plasma sintering (SPS), or field assisted sintering technique (FAST), is a newly discovered old technique which recently has been used for superfast densification of ceramic powders [1–3]. This hot-pressing process which is characterized by simultaneous application of load and pulsed high dc current densities was traditionally used for compaction and plastic deformation of metallic powders and billets. It is now in progress for superfast consolidation of monolithic and composite ceramic powders. The very short SPS durations, of the order of a few minutes, are most significant during which the densification processes go to completion [3]. This arises from the extremely high heating and cooling rates by the electrical current passage. Therefore, this method has special advantages for the fabrication of bulk nanocrystalline metals and ceramics [4, 5], joining of dissimilar materials [6], preservation of metastable microstructures [7, 8] as well as internal interfaces [9].

## Overview on conventional sintering

The sintering of powder compacts to full density is well treated theoretically and experimentally. Many atomic transport mechanisms participate in sintering and densification. The main transport mechanisms are surface, grain boundary, and lattice diffusion, as well as evaporation–condensation and viscous flow. While all these mechanisms can contribute to sintering and increasing the powder compact rigidity, only a few may be associated with its densification. In this respect, surface diffusion and evaporation–condensation are not considered the densification mechanisms, but rather as contributing to particle coarsening. Full

R. Chaim (✉)
Department of Materials Engineering, Technion – Israel Institute of Technology, Haifa 32000, Israel
e-mail: rchaim@technion.ac.il

densification by pore annihilation, and thus volume shrinkage, is possible only by grain boundary and lattice diffusion in crystalline powders, as well as by viscous flow in non-crystalline powders. The latter mechanisms are also associated with grain growth, as an inevitable process, especially at the final stage of sintering.

Special attention should be paid to the term of *surface diffusion*, especially in conjunction with nanocrystalline ceramic powders. During sintering, competition exists between particle coarsening and densification mechanisms that, respectively, lead either to porous structure with large grains, or to dense specimen followed by grain growth. Therefore, coarsening through surface diffusion is considered to be detrimental to full densification, especially in the nanocrystalline powder compacts.

On the other hand, the typical heating rates in the conventional sintering techniques via convection and radiation heating are of the order of 2–30 °C $min^{-1}$. Therefore, a few hours are often spent in heating the ceramic powder compact to reach its sintering temperature. Since surface diffusion is dominating at lower temperatures, compared to the densification mechanisms (grain boundary and volume diffusion), its time scale is enough for significant particle coarsening to occur. Alternatively, rapid heating to the sintering temperature, as is characteristic for the SPS technique (100–600 °C $min^{-1}$), may retain the advantage of the high specific surface at high temperatures.

In addition, although the debate is still on-going concerning the actual mechanisms responsible for the rapid densification by SPS [2, 10–12], the formation of high local surface temperatures on the particles induced by the electric spark is worth further discussion. As will be shown below, the surface term may have significant impact on ceramic powder densification by SPS.

## The SPS characteristics

Typical SPS system is a hot-pressing unit in vacuum, where the specimen is heated to the sintering temperature using dc electric current pulses. The set-up contains graphite die and punches, and sometimes carbon felt insulation. Simulation of the SPS process by combined thermal and electrical analyses was performed to evaluate the dependence of the densification on the thermal and electrical behavior of the specimen [13–16]. Such finite element analyses led to the conclusion that punches generate the majority of the heat. The specimen temperature increases due to thermal conduction of the punches. Therefore, homogeneous heating of too thick or large diameter isolating ceramic specimens at short durations may be limited, owing to the relatively low thermal conductivity of the ceramic [13–15]. At longer durations temperature gradients as high as 100°C may form, in favor of the external die surface compared to the specimen center. The electrical current was maximal at the end of the punch and almost zero in the isolator (i.e. alumina) specimen; the majority of the current was diverted to the die. In this respect, no current was converted to heat within the compact, in agreement with the plasma formation at the particle surfaces. Calculated voltage contours showed the existence of potential gradient between the top and the bottom of the specimen, which may be the cause for discharge.

Several different investigations have shown the effect of various SPS parameters and powder characteristics on the densification behavior. Multiple pulsing of the electric current was found to enhance the final density of α-alumina powders from 85 to 95% [1]. SPS of Alumina powders at 1,550 °C and 30 MPa for 10 min was systematically investigated [17]. Decrease in the alumina particle size, especially at short SPS durations, was associated with continuous increase in density. Submicrometer particle size was found to be necessary for efficient densification by SPS, especially for short SPS durations. This effect illustrates that the thermal processes responsible for densification occur mainly at the surface of the particles. Increase in the heating rate from 20 to 300 °C $min^{-1}$ had decreased the shrinkage duration of alumina from 80 to 6 min, respectively. Nevertheless, some threshold heating rate existed.

Microstructural analysis of $PbTiO_3$ with 100 nm particles subjected to SPS for only 1 min at 1,000 and 1,100 °C showed increase in the grain size by factors of 4 and 10, respectively [18]. This indicates that surface diffusion and particle coarsening occur very fast and cannot be neglected during SPS, especially in nanocrystalline powders. These and others results emphasize the importance of the high specific surfaces needed for rapid densification using SPS.

## Experimental procedures

Pure commercial nanocrystalline MgO (Nanomaterials Res. Inc., Longmont, CO) and YAG powders (Tal Materials Inc., Michigan) were used for densification by SPS. The nc-MgO powder had equiaxed polyhedral shape particles with average particle diameter of 11 nm and specific surface area 145 $m^2/g$. The main impurity was 0.01 wt% Fe. The nc-YAG powder had spherical shape particles with average particle diameter of 34 nm

and specific surface area 22 ($m^2/g$). Its composition contained 150 ppm Si, 80 ppm Cl, 60 ppm Na and 20 ppm Zr according to the ICP analysis. The dilatometric shrinkage curves were recorded at the heating rate 5 °C/min.

Sintering was performed in SPS apparatus, Dr Sinter 2050 (Sumitomo Coal Mining Co. Ltd., Japan) in Stockholm University. Generally, measured quantity of the as-received powders were poured into the graphite die with an inner diameter of 12 mm, and pre-pressed to 100 MPa before heating. The pressure was released and a low pressure of 10 MPa was applied during the heating up procedure. The pressure was increased to the working pressure (i.e. SPS pressure) of 100 MPa within 20 s after reaching the final sintering temperature (i.e. SPS temperature), and held for a constant duration (i.e. SPS duration) of either 3 min (for nc-YAG) or 5 min (for nc-MgO). The temperature was regulated by a thermocouple that was inserted into the pressing graphite die, at a distance of 2 mm from the sample. The temperature range for densification by SPS was selected based on the dilatometric shrinkage curves. The following SPS conditions were applied: average current density 200 A $cm^{-2}$, 5 V DC, and 3 ms pulse rate.

The typical relative green density of these nanocrystalline powders, compacted by cold isostatic pressing under 240 MPa pressure, was ~50%. The final densities were determined by the Archimedes method using 2-propanol as the immersion liquid.

The microstructure and the phase content of the sintered specimens were characterized using high resolution scanning electron microscopy (HRSEM, LEO Gemini 982) and X-ray diffraction (XRD, PW 1820), respectively. The grain size (diameter) was determined as the largest axis of the grain, directly from the HRSEM images. At least several hundred grains were counted for determining the grain size distribution. The nc-MgO specimens were polished using 0.25 μm diamond paste that revealed the microstructure without etching. Since the topology of the nc-MgO surfaces clearly exposed the true grain morphology, no stereological correction factors were used. However, correction factor of 1.56 was used for the grain size measured from the polished and thermally etched surfaces of the YAG specimens (at 1,250 °C for 15 min). The average grain size was used for presentation. The starting nc-MgO grain size was determined using the coarsening data from the literature (see details in Ref. [25] for nc-MgO). The original particle size was almost doubled between 700 and 800 °C. The starting nc-YAG grain size at all temperatures and before the SPS process was assumed as constant ($d_0$ = 87 nm) and was determined by 5 h annealing of a powder compact at 900 °C.

## Results

Dilatometric linear shrinkage curves of the nc-MgO and nc-YAG during the heating are shown in Fig. 1. The shrinkage in the nc-MgO compact started above 700 °C (curve (a)), where the maximal shrinkage rate (slope of the curve) occurred around 1,150 °C. The corresponding shrinkage of the nc-YAG powder started above 1,350 °C (curve (b)) and the maximal shrinkage rate was around 1,600 °C. Therefore, the corresponding SPS experiments were performed at the temperature ranges 700–800 °C for nc-MgO, and 1,250–1,500 °C for nc-YAG powders. Both powders exhibited single phase cubic structure prior to and after the SPS (Fig. 2).

### Densification of nc-MgO

The density of the nc-MgO specimens after SPS at 100 MPa for 5 min between 700 and 800 °C is shown in Fig. 3a. The sintered density ranged from 91 to 96% using the density of MgO single crystal (3.582 g $cm^{-1}$) as a reference. It steadily increased with the SPS temperature increase. The density values seem to be underestimated since the specimens exhibited relatively high optical transparency [5]. An example for the microstructure of the SPS densified nc-MgO is shown in Fig. 4a. Quantitative analysis of HRSEM micrographs at different SPS temperatures showed the corresponding grain sizes between 30 and 72 nm

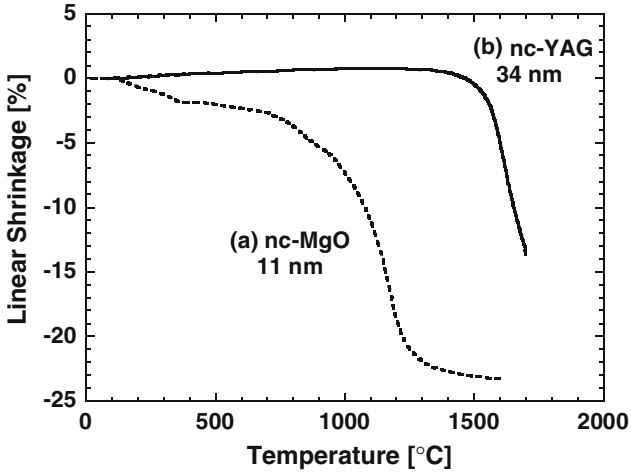


**Fig. 1** Linear shrinkage of the nanocrystalline MgO and YAG powder compacts versus temperature

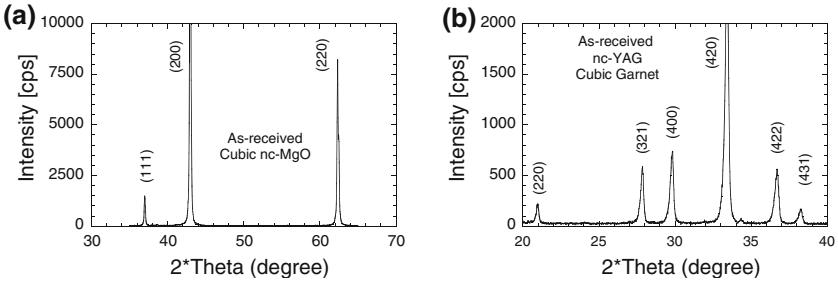


**Fig. 2** X-ray diffraction patterns of (**a**) nc-MgO and (**b**) nc-YAG powders

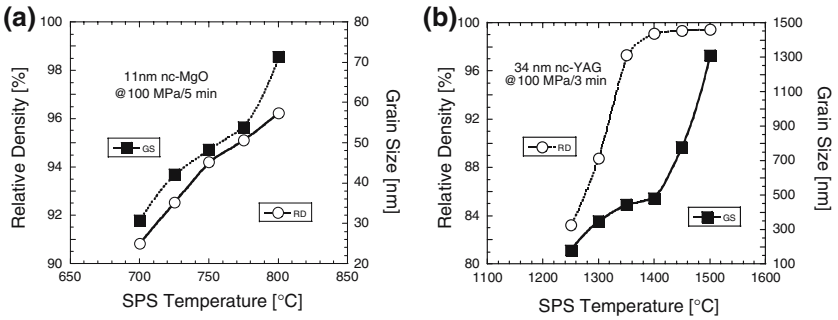


**Fig. 3** Density and grain size of (**a**) nc-MgO and (**b**) nc-YAG powder compacts versus the SPS temperature

(Fig. 3a). The grain size was also found to increase with the SPS temperature, though, in an accelerated manner at 800 °C. The grain size distribution of all the specimens exhibited log-normal character with a standard deviation equal to 50% of the average grain size. These observations confirmed the nanocrystalline character of both grains and pores in the present MgO specimens.

## Densification of nc-YAG

The relative density of the nc-YAG compacts versus the SPS temperature after 3 min at 100 MPa is shown in Fig. 3b. Sharp increase in the relative density from 83 to 99.6% was observed within the very narrow temperature range of 150 °C, between 1,250 and 1,400 °C. The corresponding grain size in this temperature range increased with temperature in a parabolic manner and was in the submicrometer range. Further increase in the SPS temperature up to 1,500 °C resulted in statistically the same highest density. Significant grain growth was observed at the SPS temperatures higher than 1,400 °C, where the grain size entered the micrometer range (Fig. 3b). The microstructure of the fracture surface (Fig. 4b) revealed tetrakaidekahedron shape micrometer size grains. The significant increase in the grain growth rate at high relative densities is often related to the change in the pore nature from continuous to isolated pores. Nevertheless, any change in the grain growth mechanism may also be responsible for a similar enhancement in the grain growth rate, as will be discussed later.

Extensive microstructural investigation was performed on the different specimens in order to reveal the densification mechanism and grain growth at various stages, the highlights of which were summarized below. The change in the volume fraction of the porosity and its continuity were well observed.

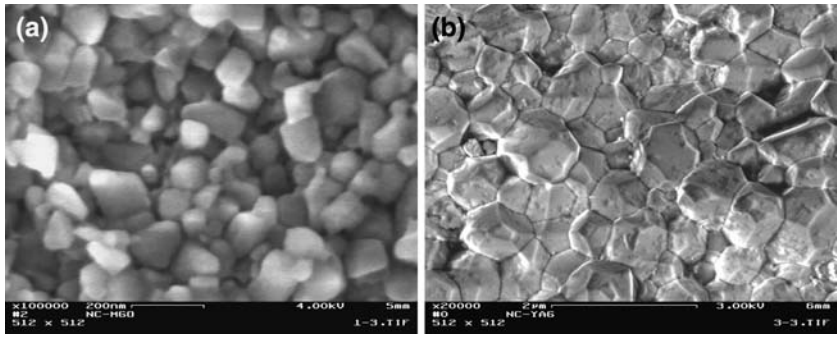


**Fig. 4** HRSEM images of (**a**) polished surface of 95% dense nc-MgO and (**b**) fracture surface of 100% dense micrometer size YAG after SPS

Two distinct microstructural features clearly pointed to the densification and grain growth mechanisms. First, a few large single crystals with faceted morphologies were formed within the residual cavities as shown in Fig. 5a. Formation of such crystals with perfect facetted morphology may be envisaged via evaporation–condensation mechanism. Moreover, evaporation–condensation of YAG is expected to occur in the presence of the melted layer at the particle surfaces around the closed cavity. Since the vapor pressure of YAG is relatively low at the melting point [19], evaporation–condensation cannot be regarded as a dominating mechanism for sintering and densification. However, surface melting of the YAG particles is necessary for these YAG crystals to grow by the evaporation–condensation mechanism. However, the second microstructural feature that characterized the bulk of the specimens was the formation of nano-grain clusters within the larger grains (Fig. 5b). This microstructure is an evidence for densification and grain growth by grain rotation mechanism [20] where the grains are nanometric in size, as will be discussed below. Increase in the grain cluster size (with SPS temperature and duration) decreases the tendency for grain rotation due to increase in the accommodation strains associated with the grain shape changes. The different surface relieves visible within the larger grains and at their grain boundaries (Fig. 5b) most probably resemble two types of grain boundaries: low-angle grain boundaries (LAGB) within the nano-grain clusters and separating between the nano-grains, and high-angle grain boundaries (HAGB) separating between the larger grains. Therefore, at the final stages of densification, where high relative densities attained, further densification and grain growth will be controlled by curvature driven grain boundary migration (i.e. normal grain growth). In this respect, small pores that are located within the grains as well as at the grain boundaries (arrowed in Fig. 5b) may be annihilated only by further densification via volume or grain boundary diffusions, respectively.

## Discussion

### Densification mechanisms

#### *Nanocrystalline MgO*

Densification of MgO powders by pressureless sintering and hot-pressing was thoroughly investigated and well documented in the literature [21]. Generally, the conventional micrometer size powders need relatively high temperatures above 1,500 °C for full densification. However, the corresponding sintering temperature decreases with the decrease in the particle size. The densification temperature may further be lowered below 800 °C by hot pressing of ultrafine and nanometer size MgO powders [22, 23]. Systematic hot-pressing study of the present nc-MgO powders in the temperature range 700–800 °C showed that the plastic deformation followed by Coble creep were the dominating densification mechanisms [24]. This was in accordance with the extremely low room temperature hardness (~7 GPa) and low yield stress ~80 (MPa) of MgO between 600 and 800 °C [25]. The present SPS results of the nc-MgO powders were in reasonable agreement with calculated values using the hot isostatic pressing (HIP) model [25]. Densification up to 75% density was expected to take place by the plastic deformation, immediate to pressure application at the SPS temperature. This was followed by diffusional processes to full density. Analysis of the

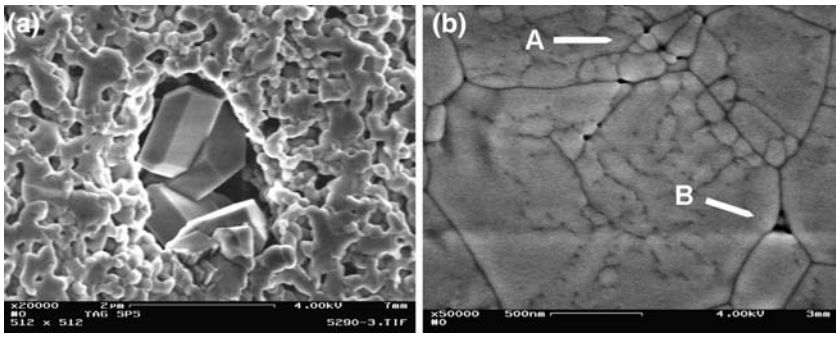


**Fig. 5** HRSEM images from the nc-YAG subjected to SPS. (**a**) The growth of the faceted YAG crystals within the cavity indicates that evaporation–condensation mechanism is active at these SPS conditions. SPS for 3 min at 1,250 °C and 100 MPa. (**b**) Densification mechanism by the nano-grain rotation, leading to dense nano-grain clusters within the large grains is exhibited. The pores within the clusters (arrowed A) and at the grain boundaries (arrowed B) are visible. SPS for 6 min at 1,400 °C and 100 MPa

hot-pressing kinetics showed the diffusion of $Mg^{2+}$ cations along the grain boundaries to be the rate controlling mechanism [24].

*Nanocrystalline YAG*

Unlike nc-MgO, densification of nc-YAG by plastic deformation necessitates extremely high stresses and temperatures due to its excellent creep resistance properties [26]. The plastic yield stress of YAG is as high as 360 (MPa) at 1,785 °C [27], and was estimated as 1 to 3–4 (GPa) at lower temperatures of 1,400 and 1,150 °C, respectively [28]. Such high stresses may barely be reached in the SPS experiments, while using the graphite dies. Alternatively, the observed microstructure of the nc-YAG subjected to SPS clearly showed crystals grown by evaporation–condensation within a few large cavities; this should be associated with formation of a liquid YAG at the particle surfaces. Therefore, densification and grain growth at the early stages of SPS takes place by nano-grain rotation to form dense nano-grain clusters. The originally HAGB's between these nano-grains converts to LAGB's by the grain rotation. The resultant strains due to the shape change may be accommodated by the viscous layer between the nano-grains. Nevertheless, this mechanism is effective only at the first and the intermediate stages of sintering, where the volume fraction of the free surfaces is high enough and the pore size is comparable to the grain size. This mechanism may not be active at the final stage of sintering, where the grain or cluster size is large and associated with much smaller isolated pores. At this stage, no free surfaces are available for the electric breakdown and for the liquid supply. Large clusters necessitate also higher accommodation strains that lower the propensity for grain rotation. Further densification and especially the grain growth should then take place by curvature driven grain boundary migration. Eventually, the LAGB's within the large grains will also be annihilated at the latter stages of densification during the normal grain growth.

In order to verify the above hypothesis, the grain size data were analyzed to reveal the possible grain growth mechanisms associated with sintering.

Grain growth by different atomistic mechanisms can be expressed using the equation:

$$d_t^n - d_0^n = kt \tag{1}$$

where

$$k = k_0 \cdot \exp\left(-\frac{Q}{RT}\right) \ (\mathrm{m^2\,s^{-1}}) \tag{2}$$

where $d_t$ and $d_0$ are the grain sizes at time $t$, and $t = 0$, respectively, $n$ is the grain growth exponent, $k_0$ is the pre-exponential constant of the diffusion coefficient, $Q$ is the activation energy for grain growth, $T$ is absolute temperature, and $R$ is the gas constant.

The value of the grain growth exponent characterizes the rate controlling process, i.e. $n = 2$ for grain growth controlled by grain boundary diffusion, versus $n = 3$ for grain growth controlled by diffusion through the bulk. The grain size data in Fig. 3b were analyzed according to Eqs. 1 and 2 and the resultant Arrhenius plots were shown in Fig. 6.

At the higher temperature range 1,400–1,500 °C, the best linear regression ($R = 0.956$) was found for $n = 2$ with the activation energy 553 ± 24 (kJ $mol^{-1}$). The pre-exponent coefficient $k_0$ is independent of the temperature and may be determined at the highest temperature where solid YAG still exists, i.e. at melting temperature of YAG ($T_m$ = 1,970 °C). Using Eqs. 1 and 2 for data extrapolated to $T = T_m$ and at $t = 180$ (s) the resultant value of the pre-exponential coefficient is $k_0 = 0.290$ ($m^2\ s^{-1}$). Therefore, the diffusion coefficient responsible for the grain growth at the higher temperature range during the SPS may be expressed by:

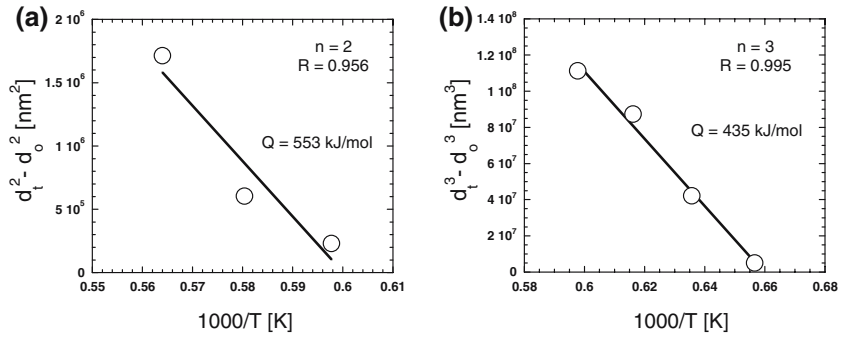


**Fig. 6** Arrhenius type plots of the YAG grain size versus inverse temperature that reveals the grain size exponents at the (**a**) higher and (**b**) lower SPS temperature ranges

$$k = 0.290 \cdot \exp\left(-\frac{553\,\mathrm{kJ\,mol^{-1}}}{RT}\right)\ (\mathrm{m^2\,s^{-1}}). \quad (3)$$

On the other hand, grain growth of pure and dense YAG fibers between 1,400 and 1,700 °C was found to follow the normal grain growth, where $n = 2$, and $Q = 540$ kJ mol$^{-1}$ [29]. Similar extrapolation of the data from [29] leads to $k_0 = 0.174$ (m$^2$ s$^{-1}$) for the diffusion coefficient responsible for normal grain growth, i.e. ionic diffusion perpendicular to the grain boundary:

$$k = 0.174 \cdot \exp\left(-\frac{540\,\mathrm{kJ\,mol^{-1}}}{RT}\right)\ (\mathrm{m^2\,s^{-1}}). \quad (4)$$

Comparison between Eqs. 3 and 4 indicates very close activation energies as well as the pre-exponential constants. The activation energy for diffusion of $Yb^{3+}$ cation (which is comparable to $Y^{3+}$ self diffusion) along the grain boundaries in YAG was reported as 530 (kJ mol$^{-1}$) [30], very close to that found in the present work. On the other hand, very similar activation energy of 540 (kJ mol$^{-1}$) [31] and close activation energy of 565 ± 85 (kJ mol$^{-1}$) [30] were also reported for volume diffusion of $Yb^{3+}$ cations using YAG single crystals and polycrystals, respectively.

Calculating the diffusion coefficients at 1,400 °C using Eqs. 3 and 4 results, respectively, in values of $1.57 \times 10^{-18}$ (m$^2$ s$^{-1}$) and $2.39 \times 10^{-18}$ (m$^2$ s$^{-1}$) which are almost identical to the value of $2.06 \times 10^{-18}$ (m$^2$ s$^{-1}$) obtained at the same temperature for volume diffusion of $Yb^{3+}$ in YAG single crystal [31]. Very close activation energy of 549 (kJ mol$^{-1}$) and diffusion coefficient of $1.50 \times 10^{-18}$ (m$^2$ s$^{-1}$) were calculated using the Nabarro–Herring equation for creep data of polycrystalline YAG at 1,400 °C [32]. All these findings indicate that the grain growth is actually controlled by volume diffusion of the slowest cation (i.e. $Y^{3+}$) towards the grain boundary. Thus, the calculated diffusion coefficients from Eqs. 3 and 4 represent the diffusion coefficient of $Y^{3+}$ perpendicular to the grain boundary, and are comparable to its volume diffusion.

These facts indicate that grain growth at the higher temperature range takes place by $Y^{3+}$ diffusion perpendicular to the grain boundary which is manifested by normal (parabolic) grain growth law. This is in agreement with both the ambipolar diffusion of $Y^{3+}$ and almost fully dense nature of the specimens (above 99%), where continuous grain boundary network is present.

Different grain growth behavior was found at the lower temperature range 1,250–1,400 °C. The best linear regression ($R = 0.995$) was found for $n = 3$ with the activation energy of 435 ± 11 (kJ mol$^{-1}$). The grain growth exponent $n = 3$ is characteristic of grain growth processes controlled by mass transport through the volume [33]. However, it should be noted that at this temperature range the specimens is not fully dense and the average grain size is below 500 nm (Fig. 3b). In addition, some evidence for particle surface melting was observed (Fig. 5a). Let assume that application of the pulsed dc current leads to accumulation of electric charge on the ceramic particle surfaces that in turn initiate a spark by a surface discharge and to plasma formation (ionized gas colliding to the particle surfaces). Such plasma is expected to induce local surface temperatures as high as the melting temperature of the YAG particles (~1,970 °C). At the same time, these particle surfaces are subjected to applied stress, thus allow melt continuity across the particle–particle interfaces. The thickness of the melt at such interfaces may be of a few atomic distances, comparable to twice the surface diffusion depth of the particle. In such a case, densification and grain growth of the nano-grains may proceed by grain rotation and its shape accommodation aided by its surrounding viscous layer. Deformation by grain boundary rotation is considered as a viscous process [34] and the corresponding grain growth may be treated by diffusion through the liquid phase. In order to either verify or negate this possibility, the diffusion coefficient that may be responsible for grain growth in the lower temperature range should be estimated as is described below.

Grain growth controlled by diffusion through the liquid phase may be expressed as [35]:

$$d_t^3 - d_0^3 = k_\mathrm{D} \cdot t \quad (5)$$

where

$$k_\mathrm{D} = \frac{8\gamma_\mathrm{SL}\Omega D_\mathrm{V} C_0}{9RT} \cdot f \quad (6)$$

where $\gamma_\mathrm{SL}$ is the solid–liquid interfacial energy, $\Omega$ is the atomic volume of the diffusing species, $D_\mathrm{V}$ is the volume diffusion coefficient, and $f$ is the volume fraction of the solid.

Assuming that the particle surfaces contain a ''viscous'' layer of constant thickness, the volume fraction of this layer may be calculated for tetrakaidekahedron morphology [36]. For 34 nm in diameter YAG nanoparticles and layer thickness

$\delta$ = 1 nm, the volume fraction of the ''viscous'' layer is ~10%, leaving the volume fraction of the solid particle to be $f$ = 0.9.

The interfacial energy $\gamma_{SL}$ is expected to be relatively small, due to the identical composition of the solid and liquid, and thus the full wetting (spreading) of the solid by the liquid. In such a case, the Young's equation for the surface energies in equilibrium is:

$$\gamma_{SV} = \gamma_{SL} + \gamma_{LV} \cdot \cos(\theta) \quad (7)$$

where indices S, L, and V refer to solid, liquid and vapor, respectively, and $\theta$ is the wetting angle.

For full wetting, $\theta$ tends to zero, thus $\cos(\theta) \rightarrow 1$. Since the surface energies are positive, $\gamma_{SL}$ cannot be greater than $\gamma_{LV}$. The latter $\gamma_{LV}$ for YAG was determined to be 0.781 (J m$^{-2}$) [37]. Therefore, it is reasonable to use a lower value for $\gamma_{SL}$, i.e. 0.5 (J m$^{-2}$), close to that reported for molten glass on alumina [38].

Solubility of solid YAG in liquid YAG is 100%. However, the ionic specie that may control the diffusion rate in the 'viscous' layer is the slowest ion, due to the ambipolar nature of the diffusion in oxides. The slowest ion in crystalline YAG was found to be $Y^{3+}$ cation according to diffusion and creep results [31]. Following this choice for the ''viscous'' YAG layer, the solubility of $Y^{3+}$ in stoichiometric YAG may be used, i.e. $C_0$ = 0.373. Consequently, the evaluated diffusion coefficient should then be referred to that of $Y^{3+}$ cation in 'viscous' YAG.

Using the grain size data at 1,350 °C in the lower SPS temperature range (Fig. 6b), $t$ = 180 (s), $\Omega = 8.347 \times 10^{-4}$ (m$^3$ mol$^{-1}$), the diffusion coefficient for $Y^{3+}$ through the $\delta$ = 1 nm ''viscous'' surface layer is given by:

$$D_{\text{viscous}}^{Y^{3+}} = 4.31 \times 10^{-14}\ (\text{m}^2\,\text{s}^{-1}). \quad (8)$$

In order to get an estimation for the diffusion coefficient of the $Y^{3+}$ cation in ''viscous'' YAG, one can consider diffusion of cation in liquid according to Stokes–Einstein equation:

$$D_{\text{liquid}}^{\text{cation}} = \frac{kT}{3\pi\eta \cdot r_0} \quad (9)$$

where $\eta$ is the melt viscosity and $r_0$ is the ionic radius.

Numerous crystal growth studies indicate that liquid YAG can severely be undercooled to form glass under containerless melt-process conditions [37, 39–41]. The viscosity of molten YAG around its melting temperature (1,970 °C) is of the order of 0.05 (Pa s) and was found to weakly depend on temperature, exhibiting ''fragile'' glass [37]. However, the viscosity at the lower temperature range of 1,600–1,650 K for pulling glass fibers was reported in the range of 30–300 (Pa s) [39]. Therefore, using the value of 300 (Pa s) at 1,327 °C (i.e. 1,600 K) together with the ionic radius of $Y^{3+}$ as 0.104 nm in Eq. 9 results in a diffusion coefficient of $7.5 \times 10^{-14}$ (m$^2$ s$^{-1}$). This value is very close to the diffusion coefficient value derived in Eq. 8 for diffusion controlled grain growth through the viscous YAG. Hence, these results support the formation of liquid phase at the particle surfaces that in turn enhances the densification. The calculated activation energy, 435 ± 11 (kJ mol$^{-1}$) is very close to that of the YAG enthalpy of fusion, 420 (kJ mol$^{-1}$) [42], that is to maintain the liquid YAG at the particle surfaces during the process.

The formation of the liquid phase may also be supported by the formation of the polyhedral-shape faceted YAG single crystals within the closed cavities by the evaporation–condensation mechanism. Since the vapor pressure of YAG is relatively low at the melting point, evaporation–condensation cannot be regarded as a dominating mechanism for sintering, but by-product of the liquid formation. However, in the presence of liquid YAG, such an evaporation may be enhanced and result in the microstructure observed in Fig. 5.

## Summary of SPS mechanisms

Analysis of the density and grain size versus the SPS parameters and the observed microstructures reveal that different mechanisms dominated the fast densification to full density of nc-MgO and nc-YAG. Where nc-MgO was densified by plastic deformation immediate to the pressure application at the SPS temperature [5, 25] the nc-YAG did not plastically deform but densified via the liquid phase. In both oxides, the measured SPS temperatures were far below the melting temperatures (i.e. 0.31–0.34 $T_m$ in MgO and 0.68–0.79 $T_m$ in YAG). As was shown, the nc-YAG powder particles apparently experienced very high local surface temperatures which resulted in surface melting. Despite these differences, the rapid densification in both oxides can be described by existing densification mechanisms, such as plastic deformation (i.e. nc-MgO) and liquid phase sintering (i.e. nc-YAG).

These densification mechanisms are dictated by the fundamental properties of these oxides such as their crystal structure and defects. Magnesium oxide with the Rock-salt crystal structure and ionic bond character, is considered as a ductile ceramic, and undergoes

plastic deformation at 700 °C and 100 MPa [25]. This plasticity may be enhanced in the reducing atmosphere (partial CO atmosphere in the SPS vacuum chamber), where high concentration of oxygen vacancies may enhance the metallic character of the neighbor Mg ions [43]. The YAG crystal, on the other hand, has a Garnet crystal structure with mixed covalent–ionic bonds [44] and large Burger vector, thus barely undergoes plastic deformation even at high temperatures [45].

Observation of the present findings and other SPS experiments from the literature [1, 46–48] may point to two competing densification processes during the SPS that depend on the physical and morphological properties of the powder. Densification is controlled by plastic deformation when the applied pressure is higher than the yield stress at the SPS temperature. However, plastic deformation is absent when the particle yield stress is higher than the corresponding applied pressure. On the other hand, the main electric power in the SPS was found to be delivered by the component at zero frequency in agreement with the static nature of the applied dc field [15]. In this respect, the applied dc field with zero frequency dictates the surface space charge as a main polarization mechanism for the non-conducting ceramic particles [49]. Accumulation of this space charge by pulsed dc current and its concurrent discharge are believed to cause the ionization of the surrounding gas and plasma formation [2, 50], hence the local surface heating and melting of the powder [48].

High temperature plastic deformation due to the applied pressure is expected to increase the solid–solid (grain boundary) interfaces on the expense of the solid–gas (free surface) interfaces. This will lead to a decrease in the volume fraction of the available solid–gas interfaces, and thus diminish the space charge polarization effect. Consequently, plastic deformation mechanism may dominate in densification of ceramic particles with low yield stress. Particles with high yield stress are expected to preserve their geometry and morphology, and enhance the space charge build-up during the repeated pulsed dc current. In such ceramic particles, densification by liquid phase formation may dominate. The crossover between the two densification mechanisms depends on the SPS process parameters [46], as well as on several mechanical, physical and electrical properties of the ceramic particles and their field and temperature dependence. This crossover may also be controlled by the temperature at which the pressure is applied.

**Acknowledgements** Financial support of the Israel Ministry of Defense is gratefully acknowledged. Dr James Shen from Stockholm University is gratefully acknowledged for preparing the samples. I thank Dr Richard Ghez from Technion for the fruitful discussions.

## References

1. Groza JR, Risbud SH, Yamazaki K (1992) J Mater Res 7:2643
2. Mishra RS, Risbud SH, Mukherjee AK (1998) J Mater Res 13:86
3. Nygren M, Shen Z (2003) Solid State Sci 5:125
4. Ichikawa K, Murakami T, Nakayama Y, Miyamato S, Tokita M (2003) Mater Sci Forum 426:2375
5. Chaim R, Shen Z, Nygren M (2004) J Mater Res 19:2527
6. Liu W, Naka M (2003) Scripta mater 48:1225
7. Hun Kim K, Bo Shim K (2003) Mater Character 50:31
8. Zhan G-D, Kuntz J, Wan J, Garay J, Mukherjee AK (2003) Mater Sci Eng A 356:443
9. Jun Wu Y, Uekawa N, Kakegawa K (2003) Mater Lett 57:4088
10. Wang SW, Chen LD, Hirai T, Kang YS (1999) J Mater Sci Lett 18:1119
11. Groza JR, Garcia M, Schneider JA (2001) J Mater Res 16:286
12. Krell A, Van Bruggen MPB (2004) Bull ECerS 2:35
13. Keum YT, Jeon JH, Auh KH (2002) J Ceram Proc Res 3:195
14. Matsugi K, Kuramoto H, Hatayama T, Yanagisawa O (2004) J Mater Proc Tech 146:274
15. Anselmi-Tamburini U, Gennari S, Garay JE, Munir ZA (2005) Mater Sci Eng A 394:139
16. Vanmeensel K, Laptev A, Hennicke J, Vleugels J, Van Der Biest O (2005) Acta Mater 53:4279
17. Wang SW, Chen LD, Hirai T (2000) J Mater Res 15:982
18. Takeuchi T, Tabuchi M, Kondoh I, Tamari N, Kageyama H (2000) J Am Ceram Soc 83:541
19. Nordine PC, Weber RJK, Abadie JG (2000) Pure Appl Chem 72:2127
20. Haslam AJ, Moldovan D, Yamakov V, Wolf D, Phillpot SR, Gleiter H (2003) Acta Mater 51:2097
21. Vieira JM, Brook RJ (1984) J Am Ceram Soc 67:450
22. Itatani K, Yasuda R, Scott Howell F, Kishioka A (1997) J Mater Sci 32:2977
23. Feng Y, Agrawal D, Skandan G, Jain M (2004) Mater Lett 58:551
24. Ehre D, Gutmanas EY, Chaim R (2005) J Eur Ceram Soc 25:3579
25. Chaim R, Margulis M (2005) Mater Sci Eng A 407:180
26. Corman GS (1993) J Mater Sci Lett 12:379
27. Blumenthal WR, Philips DS (1996) J Am Ceram Soc 79:1047
28. Hay RS (1994) J Am Ceram Soc 77:1473
29. King BH, Halloran JW (1995) J Am Ceram Soc 78:2141
30. Jimenez-Melendo M, Haneda H, Nozawa H (2001) J Am Ceram Soc 84:2356
31. Cherniak DJ (1998) Phys Chem Minerals 26:156
32. Parthasarathy TA, Mah T-I, Keller K (1992) J Am Ceram Soc 75:1756
33. Rahaman MN (2003) In: Ceramic processing and sintering. Marcel Dekker Inc., New York, p 603
34. Ashby MF, Verall RA (1973) Acta Metall 21:149
35. Markhsev O, Chaim R (2003) J Mater Res 18:950
36. Chaim R (1997) J Mater Res 12:1828
37. Fratello VJ, Brandle CD (1993) J Cryst Growth 128:1006
38. Kingery WD, Bowen HK, Uhlmann DR (1976) In: Introduction to ceramics. John Wiley & Sons, New York, p 208

39. Weber RJK, Felten JJ, Cho B, Nordine PC (1998) Nature 393:769
40. Tangeman JA, Phillips BL, Nordine PC, Weber RJK (2004) J Phys Chem B 108:10663
41. Aasland S, Mcmillan PF (1994) Nature 369:633
42. Geravais M, Le Floch S, Rifflet JC, Coutures J, Coutures JP (1992) J Am Ceram Soc 75:3166
43. Finocchi F, Goniakowski J, Noguera C (1999) Phys Rev B 59:5178
44. Xu Y-N, Ching WY (1999) Phys Rev B 59:10530
45. Ji S, Martignole J (1996) J Struct Geol 18:1375
46. Shen Z, Johnsson M, Zhao Z, Nygren M (2002) J Am Ceram Soc 85:1921
47. Zhou Y, Hirao K, Yamauchi Y, Kanzaki S (2003) Scripta Mater 48:1631
48. Khor KA, Yu LG, Murakoshi Y (2005) J Eur Ceram Soc 25:1057
49. Buchanan RC (1986) In: Buchanan RC (ed) Ceramic materials in electronics. Marcel Dekker, Inc., New York, p 47
50. Gao L, Shen Z, Miyamoto H, Nygren M (1999) J Am Ceram Soc 82:1061